Optics Letters

Differentiable pixel-super-resolution lensless imaging

NI CHEN AND EDMUND Y. LAM*

Department of Electrical and Electronic Engineering, The University of Hong Kong, Hong Kong SAR, China
*elam@eee.hku.hk

Received 16 December 2024; revised 15 January 2025; accepted 19 January 2025; posted 22 January 2025; published 4 February 2025

Conventional lensless imaging systems require complex phase diversity measurements and sequential processing steps, limiting their practical application despite their compact design. We present a differentiable end-to-end pixel-super-resolution (dPSR) technique that unifies PSR hologram synthesis, autofocusing, and complex-field reconstruction within a single optimization framework. By jointly optimizing these traditionally separate processes, our method eliminates both phase diversity requirements and error accumulation from sequential processing. Our method achieves superior position estimation accuracy (mean error 0.0282 pixels versus 0.1172 pixels with conventional methods), delivering precise autofocusing with accuracy better than 0.3 µm, and enabling a twofold resolution enhancement beyond the sensor's native pixel size. This robust performance is validated through both simulated and experimental results, including challenging phase objects and label-free cell imaging, establishing dPSR as a practical solution for high-resolution microscopy applications.

https://doi.org/10.1364/OL.552086

Introduction. Modern microscopy increasingly demands both high resolution and large field-of-view imaging, traditionally requiring complex optical systems with sophisticated lens arrangements. Lensless imaging offers a revolutionary alternative, achieving microscopic resolution through a remarkably simple setup: a light source and sensor positioned at a significant distance, with the sample placed close to the sensor [1]. This minimalist configuration can achieve a numerical aperture (NA) approaching 1, enabling high-resolution imaging across an exceptionally wide field of view (FOV). However, the theoretical capabilities of these systems often remain unrealized in practice. Despite advances in high-megapixel sensors, the fundamental limitation of micrometer-sized pixels constrains the achievable resolution well below the diffraction limit. Pixel-super-resolution (PSR) techniques have emerged as a crucial solution to this challenge [2,3], computationally enhancing resolution while maintaining the system's physical simplicity and cost-effectiveness. The elegance and adaptability of lensless imaging have catalyzed its adoption across diverse scientific applications. From medical imaging of cells and tissues [4] to protein crystallography [5], and from microbial monitoring [6] to environmental sensing [7], the technique's versatility continues to expand. However, several fundamental challenges limit its broader implementation.

The first major challenge lies in PSR measurement acquisition and synthesis. While the technique requires capturing multiple low-resolution images with sub-pixel shifts through mechanical scanning, precise knowledge of these shifts is not directly available. Traditional cross correlation-based image registration methods often prove unreliable, particularly when dealing with holographic data or noisy measurements. This uncertainty in position estimation propagates through subsequent processing steps, compromising final image quality.

A second critical challenge involves accurate autofocusing—determining the precise sample-to-sensor distance crucial for image reconstruction. Conventional autofocusing methods, whether based on spatial domain edge detection [8,9] or frequency domain analysis [9], struggle with the unique characteristics of lensless imaging. The presence of twin-image artifacts, combined with varying sample properties such as low absorption or large phase delays, makes robust autofocusing particularly challenging [10,11].

The third fundamental challenge involves complex-field reconstruction from PSR holograms. Traditional phase retrieval approaches typically require multiple types of diversity measurements—whether through varying wavelengths [12,13], illumination angles [14,15], heights [16], or alternative techniques such as coded masks [17] and synthetic apertures [13]. While various optimization methods exist [18], they all require precise autofocusing, creating a circular dependency that conventional sequential approaches struggle to resolve.

These challenges are fundamentally interconnected, yet traditional approaches handle them sequentially [19]. Each step introduces errors that propagate through the pipeline, significantly affecting the final reconstruction quality [20].

Method. Drawing inspiration from differentiable imaging [21,22], we propose a differentiable end-to-end pixel-super-resolution (dPSR) technique that unifies these three traditionally separate processes into a single optimization framework. This integrated approach overcomes the limitations inherent in sequential processing methods. By leveraging automatic differentiation, we simultaneously optimize the sample's complex field, scanning positions, and sample-to-sensor distance. Our dPSR approach builds upon a carefully designed experimental configuration that maximizes measurement quality while

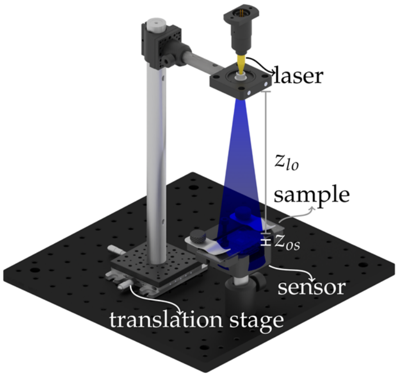

Fig. 1. Schematic of the lensless pixel-super-resolution imaging system.

maintaining system simplicity. The setup, illustrated in Fig. 1, employs a computer-controlled light source mounted on an x–y translation stage. The sample is positioned between the source and sensor, with the source-to-sample distance (z_{lo}) significantly exceeding the sample-to-sensor distance (z_{os}). This geometry ensures approximately uniform illumination while enabling high-resolution capture of the resulting diffraction patterns.

Mathematical model of the PSR lensless imaging. We formulate lensless PSR imaging as a function of three key parameters: the high-resolution complex field of the target sample (u), the sample-to-sensor distance (z), and the scanning location of each measurement (r_n, where $r_n = (x_n, y_n)$). The n-th captured image is expressed as follows:

$$y_n = f\left(u\left(r_n\right), z\right) = \mathcal{S}_{down}\left|\mathcal{P}\left(u\left(r_n\right), z\right)\right|^2. \quad \textbf{(1)}$$

The wave propagation operator $\mathcal{P}(\cdot)$ models how light travels from the sample to the sensor through convolution with the free-space point spread function, implemented using the angular spectrum method [23]. The sensor's pixel-wise sampling process is represented by $\mathcal{S}_{down}$ [16,24], which accounts for the discretization of the continuous optical field. The squared magnitude operation $|\cdot|^2$ reflects the fact that our measurements capture only intensity information, losing direct phase measurements.

Taking the first measurement y_0 as the reference, the n-th measurement y_n can be expressed as translating the first measurement by $r_n - r_0$. The translation operation can be expressed using the following expression:

$$u\left(r_n\right) = \mathcal{F}^{-1}\{\mathcal{F}\{u(r_1)\} \times \exp\left[j2\pi \cdot (r_n - r_1) \cdot f_r\right]\}. \quad \textbf{(2)}$$

Here, f_r represent the frequency coordinates along the x and y axes and $\mathcal{F}$ and $\mathcal{F}^{-1}$ denote the Fourier transform and its inverse, respectively. This formulation efficiently models sample translations through phase shifts in the frequency domain, avoiding the need for spatial interpolation. This complete forward model enables simulation of the entire imaging process, from sample translation through wave propagation to sensor sampling. The differentiable nature of each component proves crucial for our optimization approach, allowing us to compute gradients through the entire imaging process.

Differentiable optimization. The core innovation of our approach lies in simultaneously optimizing the sample reconstruction (u), sample-to-sensor distance (z), and scanning positions ($r = r_1, \ldots, r_N$). We formulate this joint optimization through a comprehensive error metric combining four complementary terms:

$$\begin{aligned}\mathcal{L}(u, z, r) = &\frac{1}{N}\sum_{n=1}^{N}\|f(u(r_n), z) - y_n\|^2\\ &+ \beta_0\frac{1}{N_xN_y}\sum|\nabla^2|\mathcal{P}(u(r_1), z)|^2|\\ &+ \beta_1\mathbb{R}_{\ell_1}(u(r_1)) + \beta_2\mathbb{R}_{\mathrm{TV}}(u(r_1)).\end{aligned} \quad \textbf{(3)}$$

The first term, $\frac{1}{N}\sum_{n=1}^{N}|f(u(r_n),, z) - y_n|^2$, represents the data fidelity constraint. This term ensures that the output of the forward model matches the experimental measurements. The second term, $\beta_0\frac{1}{N_xN_y}\sum|\nabla^2|\mathcal{P}(u(r_1),, z)|^2|$, enhances high-resolution features in the reconstruction. The third component introduces sparsity promotion through the l_1 norm $\beta_1\mathbb{R}_{\ell_1}(u(r_1))$ [22]. Finally, the total variation (TV) norm term $\beta_2\mathbb{R}_{\mathrm{TV}}(u(r_1))$ helps suppress experimental noise while preserving important edge features in the reconstruction. The balance between these four terms, controlled by the parameters β_0, β_1, and β_2, can be tuned to optimize performance for different types of samples and noise conditions.

Despite the nonlinear and non-convex nature of this optimization problem, the differentiability of our forward model enables efficient solution through gradient descent, as detailed in Algorithm 1. The algorithm jointly updates all parameters through automatic differentiation, with the imaging model evolving alongside parameter updates until convergence. This approach fundamentally differs from traditional sequential methods, eliminating intermediate PSR hologram synthesis and separate autofocusing steps in favor of direct optimization of the final high-resolution image.

Numerical experiments for error analysis. We conducted systematic numerical experiments to validate our method's performance and understand its behavior under varying imaging conditions. Our analysis focused on two critical aspects of lensless imaging: autofocusing accuracy and scanning position estimation, particularly challenging when dealing with samples exhibiting both amplitude and phase variations.

For these experiments, we carefully designed a transmission function that mimics realistic imaging conditions. The object's transmission characteristics are modeled as $t_o = \exp(-\alpha_{\max} \cdot I) \times \exp(j\phi_{\max} \cdot I)$, where I represents a normalized gray-scale image ranging from 0 to 1. The parameters $\alpha_{\max}$ and $\phi_{\max}$ control the

Algorithm 1. Differentiable lensless PSR solver

function RECONSTRUCT SAMPLE AND SYSTEM PARAMETERS($\boldsymbol{y}$)
  Initialize $\{\boldsymbol{u}^0, z^0, \boldsymbol{r}^0\}$; ▷ Initialization
  $f^0 \leftarrow f(\cdot, z^0, \boldsymbol{r}^n)$; ▷ Initialization of the forward imaging model
  while not converged **do** ▷ Iteration
    $\boldsymbol{u}^{k+1}, z^{k+1}, \boldsymbol{r}^{k+1} \leftarrow \arg\min_{\boldsymbol{u}, z, \boldsymbol{r}^k} \mathcal{L}(\boldsymbol{u}^k, z^k, \boldsymbol{r}^k)$; ▷ update with automatic differentiation
    $f^{k+1} \leftarrow f(\cdot, z^{k+1}, \boldsymbol{r}^{k+1})$; ▷ Imaging model update
  return $\{\boldsymbol{u}^K, z^K, \boldsymbol{r}^K\}$; ▷ At final iteration K

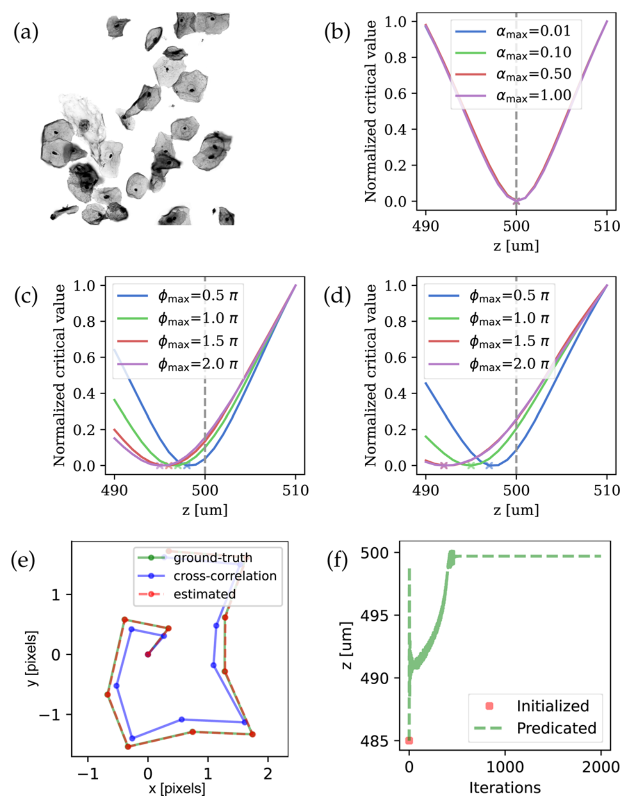

Fig. 2. Numerical evaluation of autofocusing and position estimation performance. (a) is the image used in the simulation. Autofocusing performance analysis using the Laplacian metric for (b) pure absorption, (c) pure phase, and (d) complex-amplitude sample (α_{max} = 0.1). (e) Comparison of scanning position estimation between cross correlation method (blue dots) and our dPSR approach (red dots) relative to true positions (green dots). (f) Convergence of sample-to-sensor distance estimation during optimization.

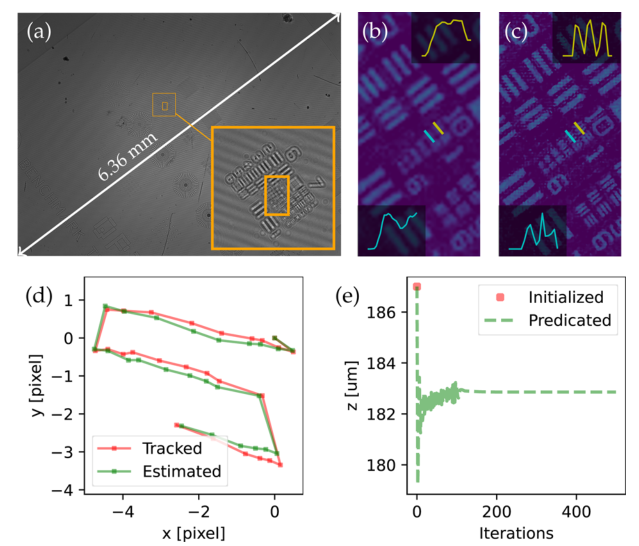

Fig. 3. Experimental validation using a phase-type USAF resolution test chart. (a) Raw holographic measurement. (b) Reconstruction from a single measurement. (c) Enhanced reconstruction using 25 measurements. (d) Scanning position estimation showing improved accuracy of dPSR (green dots) compared to the cross correlation method (red dots). (e) Sample-to-sensor distance convergence during optimization.

maximum absorption ratio and phase delay, respectively, allowing us to explore different imaging regimes systematically. The test image used is shown in Fig. 2(a). Our simulation parameters closely match typical experimental conditions, with a light source wavelength of 405 nm. Both the sample and sensor featured a pixel size of 0.9 µm with dimensions of 512 × 512 pixels. We positioned the sample 500 µm from the sensor, creating a realistic imaging geometry.

We first investigated autofocusing behavior using the established Laplacian method [25] across propagation distances from 490 nm to 510 nm. This analysis revealed different behaviors for different sample types: Pure-amplitude objects (Fig. 2(b)) showed consistent autofocusing accuracy regardless of absorption strength, demonstrating the robustness of the method for samples dominated by amplitude. However, phase-only samples (Fig. 2(c)) exhibited increasing focusing inaccuracy with larger phase delays, highlighting a fundamental limitation of conventional methods. The challenge became most pronounced with complex-amplitude samples (α_{max} = 0.1, Fig. 2(d)), where the interplay between amplitude and phase features further complicated accurate focus determination. These results underscore a fundamental challenge in lensless imaging: The twin-image problem makes distinguishing between focused and defocused states particularly difficult. Although strong absorption features create clear amplitude distributions that aid in focusing, phase-dominated samples lack such distinct markers, especially problematic when phase variations are large.

To evaluate the effectiveness of our method, we tested dPSR using a complex sample with α_{max} = 0.1 and $\phi_{max} = \pi$. Using 11 scanning positions (Fig. 2(e), green dots), we compared the accuracy of position estimation between conventional cross correlation methods and our approach. The cross correlation method achieved a mean absolute error of 0.1172 pixels (blue dots), while dPSR significantly improved the accuracy to 0.0282 pixels (red dots). Moreover, our method demonstrated excellent convergence in the estimation of sample-to-sensor distance (Fig. 2(f)), reaching 499.71 µm from an arbitrary initialization. This accurate distance determination, combined with superior position estimation, enables robust reconstruction even for challenging samples with significant phase components.

Optical experiments. To validate our method under real-world conditions, we developed an experimental setup that leverages high-resolution imaging capabilities while maintaining the simplicity of the system. Our setup employs a monochromatic CMOS sensor (Jiangsu Team One Intelligent Technology Co., Ltd.) with a pixel size of 0.9 µm and a resolution of 5664 × 4256 pixels, providing an expansive field of view (FOV) of 5.1 mm × 3.8 mm. The illumination is provided by a Thorlabs LP405C1 source operating at a central wavelength of 405 nm. The experimental geometry is shown in Fig. 1.

For our initial validation, we examined a phase-type USAF resolution test chart from Benchmark Optics. The raw measurement data, shown in Fig. 3(a), reveals the holographic interference patterns characteristic of our lensless setup. We focused our reconstruction efforts on the central patch region to demonstrate the resolution enhancement capabilities of our method. The progression from single measurement reconstruction (Fig. 3(b)) to multiple measurement reconstruction using 25 acquisitions (Fig. 3(c)) clearly demonstrates the substantial improvement in

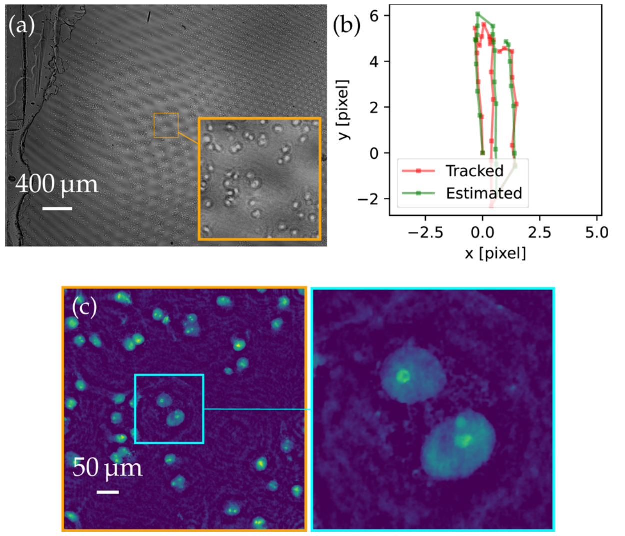

Fig. 4. High-resolution imaging of unlabeled COS-7 cells. (a) Raw holographic measurement. (b) Scanning position estimation. (c) Reconstruction from 25 measurements.

image quality achieved through our dPSR approach. The method achieves a resolution of 435 nm (group 10, element 2), representing a significant 2.0-fold improvement over the sensor's native pixel size. The accuracy of scanning position estimation proves particularly noteworthy, as illustrated in Fig. 3(d). Our method demonstrates markedly better accuracy compared to traditional cross correlation analysis, maintaining precise position tracking throughout the measurement sequence. The sample-to-sensor distance estimation, shown in Fig. 3(e), exhibits stable convergence, crucial for accurate phase retrieval in the lensless configuration.

To demonstrate the practical utility of our method for biological imaging, we conducted experiments with unlabeled COS7 cells. Figure 4(a) presents the unprocessed raw image data, while Fig. 4(c) shows the reconstruction achieved using 25 distinct measurements. The reconstructed images reveal remarkable detail of cellular structures, particularly the nuclei, without requiring any chemical labeling or staining. This capability represents a significant advantage for live cell imaging applications, where noninvasive observation is crucial for maintaining cellular viability and natural behavior.

This series of experimental results not only validates the theoretical principles underlying our dPSR method but also demonstrates its practical effectiveness in real-world imaging scenarios. The ability to achieve sub-micron resolution while maintaining a simple, lens-free setup opens new possibilities for wide-field, high-resolution biological imaging.

Conclusion. We present a differentiable end-to-end PSR lensless imaging technique that integrates hologram synthesis, autofocusing, and inverse image reconstruction into a unified framework. This approach achieves high-resolution imaging with minimal measurements and eliminates the need for phase diversity in phase retrieval. The joint optimization of scanning positions, sample-to-sensor distance, and sample reconstruction enables flexible scanning strategies. Our experimental results demonstrate a twofold resolution improvement over the sensor pixel size while maintaining system simplicity. It is important to note that while rapid scene dynamics can impact the multiple capture requirements of PSR, this limitation can potentially be addressed by incorporating dynamic scene modeling into the forward propagation model. By explicitly accounting for temporal evolution within the mathematical framework, the system could adapt to and compensate for scene changes during the capture sequence [26]. Looking forward, this framework could potentially accommodate full 3D scanning movements, which may further enhance measurement diversity and imaging performance.

Funding. Hong Kong Research Grants Council (GRF 17201822).

Acknowledgment. Ni Chen expresses sincere gratitude to Prof. Chao Zuo, Yang Chen, and Xuejuan Wu for sharing the data and to Prof. David J. Brady for offering valuable insights and perspectives. The work is supported in part by the Hong Kong Research Grants Council (GRF 17201822).

Disclosures. The authors declare no conflicts of interest.

Data availability. Data underlying the results presented in this paper are not publicly available but may be obtained from the authors upon reasonable request.

REFERENCES

1. E. McLeod and A. Ozcan, Phys. Today **70**, 50 (2017).
2. W. Bishara, T.-W. Su, A. F. Coskun, *et al.*, Opt. Express **18**, 11181 (2010).
3. A. Greenbaum and A. Ozcan, Opt. Express **20**, 3129 (2012).
4. C. J. Potter, Y. Hu, Z. Xiong, *et al.*, Lab Chip **22**, 3744 (2022).
5. M. U. Daloglu, A. Ray, M. J. Collazo, *et al.*, APL Photonics **4**, 1 (2019).
6. S. Jiang, C. Guo, Z. Bian, *et al.*, Biosens. Bioelectron. **196**, 113699 (2022).
7. Y. Wu and A. Ozcan, Methods **136**, 4 (2018).
8. F. Dubois, C. Schockaert, N. Callens, *et al.*, Opt. Express **14**, 5895 (2006).
9. P. Langehanenberg, B. Kemper, D. Dirksen, *et al.*, Appl. Opt. **47**, D176 (2008).
10. M. Trusiak, J.-A. Picazo-Bueno, P. Zdankowski, *et al.*, Opt. Lasers Eng. **134**, 106195 (2020).
11. Y. Wu, L. Lu, J. Zhang, *et al.*, Front. Phys. **9**, 1 (2021).
12. R. W. Gerchberg, Optik **35**, 237 (1972).
13. W. Luo, Y. Zhang, A. Feizi, *et al.*, Light: Sci. Appl. **5**, e16060 (2015).
14. Y. Guo, R. Guo, P. Qi, *et al.*, Opt. Lett. **47**, 1847 (2022).
15. Y. Zhou, J. Wu, J. Suo, *et al.*, Opt. Express **26**, 21418 (2018).
16. J. Zhang, J. Sun, Q. Chen, *et al.*, IEEE Trans. Comput. Imaging **6**, 697 (2020).
17. Z. Zhang, Y. Zhou, S. Jiang, *et al.*, APL Photonics **3**, 060803 (2018).
18. Y. Gao and L. Cao, Opt. Lett. **45**, 6807 (2020).
19. Z. Wu, G. Chen, S. Liu, *et al.*, Opt. Lasers Eng. **184**, 108597 (2025).
20. J. Zhang, J. Sun, Q. Chen, *et al.*, Sci. Rep. **7**, 1 (2017).
21. N. Chen, L. Cao, T.-C. Poon, *et al.*, Adv. Phys. Res. **2**, 1 (2023).
22. N. Chen, C. Wang, and W. Heidrich, Laser Photonics Rev. **17**, 1 (2023).
23. J. W. Goodman, *Introduction to Fourier Optics* (W.H. Freeman, Macmillan Learning, 2017).
24. Y. Gao and L. Cao, Opt. Express **29**, 28805 (2021).
25. S. Jiang, C. Guo, P. Song, *et al.*, ACS Photonics **8**, 3261 (2021).
26. Y. Wu, J. Wang, S. Thoroddsen, *et al.*, IEEE Trans. Ind. Inf. **1**, 1 (2024).